

# Forming the local starburst galaxy Haro 11 through hydrodynamical merger simulations

Timmy Ejdetjärn<sup>1\*</sup>, Oscar Agertz<sup>2</sup>, Florent Renaud<sup>3,4</sup>, Göran Östlin<sup>1</sup>,  
Alexandra Le Reste<sup>5</sup>, Angela Adamo<sup>1</sup>

<sup>1</sup>*Oskar Klein Centre, Department of Astronomy, Stockholm University, 106 91 Stockholm, Sweden*

<sup>2</sup>*Department of Astronomy and Theoretical Physics, Lund Observatory, Box 43, SE-221 00 Lund, Sweden*

<sup>3</sup>*Observatoire Astronomique de Strasbourg, Université de Strasbourg, CNRS UMR 7550, F-67000 Strasbourg, France*

<sup>4</sup>*University of Strasbourg Institute for Advanced Study, 5 allée du Général Rouvillois, F-67083 Strasbourg, France*

<sup>5</sup>*Minnesota Institute for Astrophysics, School of Physics & Astronomy, University of Minnesota, 116 Church St. SE, Minneapolis, MN 55455, USA*

Accepted XXX. Received YYY; in original form ZZZ

## ABSTRACT

Haro 11 is the closest known Lyman continuum leaking galaxy and serves as an important laboratory for studying the escape of Lyman continuum radiation. The galaxy is a metal-poor, starburst galaxy believed to be undergoing a merger that might help facilitate the escape of radiation. In this study, we carry out a large suite of numerical simulations of a merger between two disc galaxies, to study possible origins of Haro 11 and understand under which conditions various features of the galaxy are formed. By varying galaxy parameters describing the orbital configurations, masses, and their inclination, we perform a total of  $\sim 500$  simulations. We demonstrate that a two-disc galaxy merger is able to reproduce key, observed features of Haro 11, including its morphology, gas kinematics, star formation history, and stellar population ages and masses. We also find that small parameter variations have minimal impact on the orbits and resulting galaxy properties. In particular, we present a fiducial Haro 11 model that produces the single observed tidal tail, the presence of three stellar knots, and inner gas morphology and kinematics. By performing mock observations, we compare with the results of observational data and discuss possible origins for various features. Furthermore, we present newly gathered observational data that confirms the presence of a stellar tidal tail with similar length and direction as our simulations.

**Key words:** galaxies: individual (Haro 11) - galaxies: evolution - galaxies: interactions - galaxies: star formation - galaxies: starburst - methods: numerical

## 1 INTRODUCTION

Understanding the impact of in-situ and external mechanisms on the evolution of galaxies remains a central challenge in extragalactic astronomy. Galaxy interactions and mergers are significant events in the formation history of a galaxy, being drivers of starbursts and morphological transformations, with ramifications for massive star cluster formation and the escape of ionising radiation (e.g. Kostyuk & Ciardi 2024). Thus, knowing the specific scenario of a galaxy merger enables a deeper insight into the aforementioned physical mechanisms at work within the galaxy.

Blue compact dwarfs/galaxies (BCD/BCG) are compact and metal-poor galaxies undergoing a period of intense starburst resulting in especially young stellar populations dominating the blue part of the spectrum of the galaxy. Most BCGs have irregular morphologies (e.g. Bergvall & Östlin 2002; Micheva et al. 2013), which would indicate current or recent close interaction and/or merger with a companion (e.g. Östlin et al. 2001; Adamo et al. 2011). This can also be inferred from tidal tails or gas debris, as well as periods of starburst.

BCGs exhibit an extreme environment of stellar and cluster formation, and due to their low metallicity, compact size, and high SFR have been suggested to be analogues of young starburst galaxies in the high- $z$  Universe (e.g. Östlin et al. 2001; Adamo et al. 2011; Sirressi et al. 2022; Gao et al. 2022); believed to contribute a significant amount of the ionisation budget during the epoch of reionisation.

Haro 11 is a local BCG/BCD that has been studied thoroughly in the UV, IR, sub-mm, radio, visible, and X-ray (e.g. Östlin et al. 1999; Bergvall et al. 2006; Adamo et al. 2010; Östlin et al. 2015; Pardy et al. 2016; Gao et al. 2022; Danekhar et al. 2024; Le Reste et al. 2024). At a distance of 88.5 Mpc (Sirressi et al. 2022), it is the closest confirmed Lyman continuum (LyC) leaker (Bergvall et al. 2006; Rivera-Thorsen et al. 2017; Östlin et al. 2021; Komarova et al. 2024) and a bright Ly $\alpha$  emitter (Hayes et al. 2007; Östlin et al. 2009). This makes Haro 11 an excellent local analogue for studying the mechanisms that facilitate the escape of ionising radiation in the high- $z$  Universe during the epoch of reionisation, such as stellar feedback and gas stripping.

The stellar population and recent starburst (e.g. Adamo et al. 2010; Sirressi et al. 2022; Chandar et al. 2023), complex gas kinematics (e.g. Östlin et al. 2001, 2015; Menacho et al. 2021; Gao et al. 2022),

\* E-mail: timmy.ejdetjarn@gmail.com

and irregular stellar and gas morphology (e.g. [Adamo et al. 2010](#); [Östlin et al. 2015](#); [Menacho et al. 2021](#)), all suggest that Haro 11 is the result of an ongoing merger. Indeed, it was only recently that the presence of a tidal tail was observed in HI emission from 21 cm observations by [Le Reste et al. \(2024\)](#), which serves as a strong indication of an ongoing merger. Applying these observations as constraints, numerical models of galaxy mergers offer an avenue to confirm if these features are consistent with specific merger scenarios and explain the origin of various other properties of Haro 11.

In order to numerically model a specific (observed) galaxy merger, a set of observational constraints that can be linked to orbital parameters are required. In particular, tidal tail features and stellar properties can yield strong constraints, but still suffer from degeneracy between parameters. However, previous numerical work of galaxy interactions have managed to pinpoint the initial orbital parameters of the progenitor galaxies that reproduce the general morphology and inherent galaxy properties. For example, simulations of the Antennae galaxies have managed to reproduce the morphology of the galaxies and their tidal tails, as well as the star formation, among other properties ([Karl et al. 2010](#); [Privon et al. 2013](#); [Renaud et al. 2015](#); [Lahén et al. 2018](#)). In [Östlin et al. \(2015, hereafter Ö15\)](#), the authors provided a qualitative comparison between the Haro 11 galaxy and the Antennae galaxies. The Antennae galaxy is undergoing a merger and the authors show it to have similar morphology and kinematics as Haro 11. Although the Antennae galaxies are more massive and have two tidal tails, the fact that they have comparable kinematics and morphology suggests their orbital parameters might be similar.

However, high-resolution simulations of specific galaxy mergers are still very limited. Even more rare are simulations of BCG/BCD ([Bekki 2008](#); [Pearson et al. 2018](#); [Zhang et al. 2020](#); [Leicester et al. 2024](#)), which are useful resources to interpret observational data and deepen our understanding about the complex physical mechanisms going on in these extreme galaxy environments. A benefit of simulations, particularly for BCGs, is the access to several observation angles, which allows study of anisotropy in radiation leaking. However, finding initial conditions that show a broad agreement across different observed features is not trivial and requires an extensive study of the parameters controlling the galaxy orbits.

In this paper, we model the merger of two disc galaxies to reproduce the general morphology and properties of the Haro 11 galaxy as observed today, and discuss a possible origin of its formation. We employ the hydrodynamical and  $N$ -body code RAMSES ([Teyssier 2002](#)) to perform a scheme of low-resolution simulation tests ( $\sim 100$  pc) of the interaction, varying the galaxy and orbital parameters until the merging galaxies' morphology resembles the morphology of Haro 11 today. We compare with observational studies of the gaseous and stellar components, e.g. star formation rate and masses, to constrain the initial conditions our model. The simulation that best represents Haro 11 observational properties is then run at the higher spatial resolution of 36 pc. We present the results of this fiducial simulation and compare the successes and shortcomings of our models and discuss its applications. Furthermore, we present newly acquired deep imaging data that show the presence of a stellar tidal feature in the direction of the HI gas tail which have been predicted by the fiducial model, corroborating the good match.

The paper is structured as follows. Section 2 details observations of Haro 11 that are useful for constraining the initial conditions of the progenitor galaxies and their orbital parameters. In Section 3 we detail our numerical approach, as well as our methodology to achieve the best match with observational data by varying orbital and galactic parameters. In Section 4 we present our fiducial model and directly compare its inner and tidal tail morphology, star formation rate, stellar

population properties, and kinematics with observational data. Section 5 summarises the results of this parameters study, highlighting parameters that are important for producing specific galaxy properties. We then discuss the agreements and mismatches between our fiducial model and observation in Section 6. Finally, we summarise and discuss our results in Section 7.

## 2 OBSERVATIONAL CONSTRAINTS

In this section, we briefly outline the key components of Haro 11 that were used to constrain and confirm the initial properties and orbital parameters of the progenitor galaxies. All of these observational constraints were considered during the formulation of our simulations' initial conditions, but not all of them used, as matching every property in detail is not feasible. The method of determining our initial conditions is explained in Section 3.2.

### 2.1 Morphological appearance

A distinct feature of Haro 11 is its three bright stellar knots A, B, and C (see left plot of Figure 1 for an image of the galaxy). The morphology of the knots indicate that both B and C have a compact stellar core, while knot A appears as more spread out. This asymmetry in the stellar distribution has lead to speculations that the progenitor galaxies are dissimilar (see Ö15). Furthermore, this figure highlights another feature: a string of gas and stars that goes between knot B and A, which then loops back up and to the side. This feature has been dubbed an 'ear' and is reminiscent of a disc arm, which could be interpreted as knot B being the centre of a disc and knot A forming within that disc (see e.g. Ö15, [Menacho et al. 2019](#)).

X-ray observations have shown emission from knot B and/or C, which implies the presence of a low-luminosity active galactic nucleus or a strongly emitting X-ray binary system ([Hayes et al. 2007](#); [Prestwich et al. 2015](#); [Gross et al. 2021](#); [Danekhar et al. 2024](#)). The possible existence of an active galactic nucleus in knot B would indicate that it was once the bulge of one of the progenitor galaxies. This is because a massive black hole, such as an active galactic nucleus, would not have had sufficient time or mass to form outside the galactic centres during this interaction. Although, it is possible that the black hole was ejected during a previous interaction (see e.g. [Condon et al. 2017](#), and references therein). If knot B is found to contain an AGN, it imposes a morphological constraint on the current positions of the progenitor galaxies' centres. However, this is not conclusive as the black hole could have been ejected during previous interactions.

[Le Reste et al. \(2024\)](#) presented observations of the 21 cm HI line using the MEERKAT telescope, which uncovered the presence of a tidal tail extending approximately 40 kpc from the East side of the galaxy. The detection of a single tidal tail suggests that one of the galaxies is a disc undergoing prograde motion during the interaction. A prograde orbit has its (disc) rotation aligned with the orbital path of the object it is interacting with. This results in a concentrated region of the disc experiencing the same tidal forces for a longer duration, which yields more pronounced tidal stripping (see Section 3 in [Duc & Renaud 2013](#), for details and illustrations). In contrast, a retrograde motion, which has the opposite spin direction as prograde, has a more brief close interaction throughout the disc, resulting in a weaker (or no) tidal tail. Additionally, an elliptical galaxy has no axisymmetric rotation (disc) and is unaffected by the stripping from this alignment effect.

Other than the morphological features, Haro 11 exhibits complex

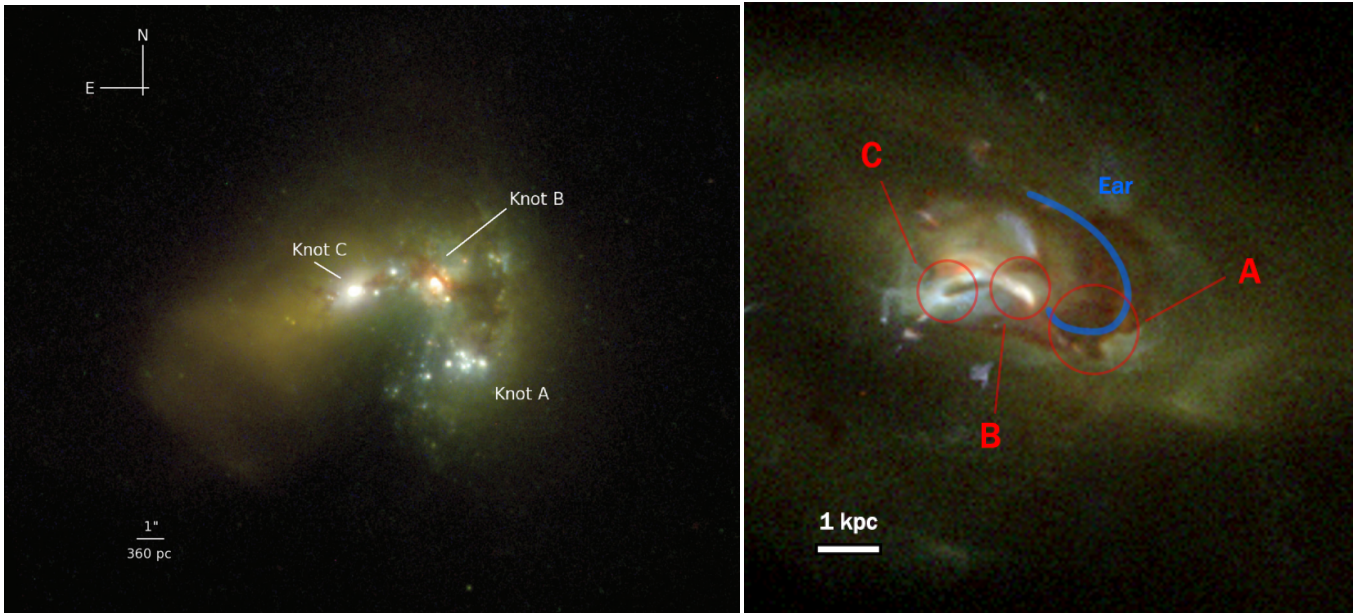


**Figure 1.** *Left:* Image of Haro 11 from [Adamo et al. \(2010\)](#), taken by HST with the waveband filters 220W, 435W, and 814W. *Right:* Mock observations of the simulated galaxy, applying the same HST filters. Details of how this mock image was produced is described in Section 4.2. Both images are of the same spatial size and resolution.

kinematics that is common in mergers. The most direct approach for comparison is to compare how different morphological parts of the galaxy move. For example through velocity maps of the inner morphology (e.g. the motion of the gas/dust ear towards us) or the expansion of the tidal tail. Additionally, there are also conical features in the ionised gas around the knots that show clear filaments and outflows ([Menacho et al. 2021](#)), suggested to be caused by feedback. As the features of feedback are too detailed and occur spuriously, they can not be directly compared with simulations. However, analysing the average properties of ionised gas and outflows could offer useful comparisons, but this is not within the scope of this project.

## 2.2 Recent star formation history

Haro 11 is currently undergoing a strong starburst with a star formation rate (SFR) upwards of  $\lesssim 30 M_{\odot} \text{ yr}^{-1}$  ([Hayes et al. 2007](#); [Adamo et al. 2010](#); [Madden et al. 2013](#); [MacHattie et al. 2014](#); [Gao et al. 2022](#)). Recently, [Sirressi et al. \(2022\)](#), see also [Adamo et al. 2010](#)) used spectra to analyse the spectral energy distribution of the three knots in Haro 11 and determined that the energy budget is best modelled by three distinct stellar age populations: 1 – 4 Myr, 4 – 40 Myr, and 40 – 100 Myr. From their analysis they estimate the stellar mass in each knot for the different ages at the range  $10^6 - 10^8 M_{\odot}$ .

One of the most significant features of Haro 11 is the leakage of Lyman continuum (LyC) radiation, making it the closest known LyC leaker ([Bergvall et al. 2006](#)). The origin of this radiation has predominantly come from knot B and C ([Prestwich et al. 2015](#); [Gross et al. 2021](#); [Östlin et al. 2021](#); [Komarova et al. 2024](#); [Danekhar et al. 2024](#)), with [Komarova et al. \(2024\)](#) reporting knot B to have a higher LyC production but lower escape fraction. While radiative transfer is beyond the scope of this study (but will be addressed in [Ejdetjärn et al. in prep.](#)), the presence of LyC radiation indicates an absence of gas in this region, toward knot C. This depletion could be the result of several mechanisms: gas being stripped during the interaction between galaxies ([Le Reste et al. 2024](#); [Kostyuk & Ciardi 2024](#)),

starburst causing an increase in stellar feedback effects (e.g. [Bergvall et al. 2013](#)), or it may be linked to the intrinsic characteristics of the progenitor galaxies (e.g. dust-poor). Based on this, some authors have proposed that Haro 11’s progenitors could have been a dwarf disc galaxy and a less gas-rich galaxy, such as a dwarf spheroidal galaxy (e.g. [Adamo et al. 2010](#); [Östlin et al. 2015](#); [Menacho et al. 2021](#)).

Extending the analysis beyond the three knots, some observations find notable stellar populations around  $\gtrsim 100$  Myr, and as old as 1 Gyr ([Chandar et al. 2023](#); [Papaderos & Östlin 2023](#)). Relevant for this study, build-up of stellar masses at specific ages in galaxies undergoing a merger might indicate starburst events triggered by close passages during the interactions (e.g. [Renaud et al. 2014a](#)). These ages can then serve as constraints for the time between the interactions in our simulated merger.

## 2.3 Gas fraction

The gas mass around the central part of Haro 11 has been estimated for the molecular  $M_{\text{H}_2} = 2.5 \times 10^8 - 3.8 \times 10^9 M_{\odot}$  ([Cormier et al. 2014](#); [Gao et al. 2022](#)), neutral HI  $M_{\text{HI}} = 0.5 \times 10^9 M_{\odot}$  ([MacHattie et al. 2014](#); [Pardy et al. 2016](#); [Le Reste et al. 2024](#)), and ionised  $M_{\text{H}\alpha} = 1.4 \times 10^9 M_{\odot}$  ([Menacho et al. 2019](#)) gas phases. The stellar mass is around  $M_{*} = 1.6 \times 10^{10} M_{\odot}$  (Ö15), which yields a total gas fraction  $f_{\text{g}} \sim 14 - 27\%$ ; depending on the molecular mass. The neutral HI mass was recently reassessed by [Le Reste et al. \(2024\)](#), who showed that previous observations had not been sensitive enough to detect the tidal tail, which they note makes up  $45^{+19}_{-21}\%$  of the total HI mass,  $M_{\text{HI}} = 1.11 \times 10^9 M_{\odot}$ . The detection of a stellar tidal tail could possibly change the galaxy’s gas fraction further. While the mass of the various gas phases provide weak constraints, due to the sensitivity to specific feedback and star formation models, the total gas mass and gas fraction are viable for us to match.

**Table 1.** The initial mass and size properties of the two progenitor galaxies. One of the galaxies is initialised with a rotation corresponding to a prograde interaction while the other has a retrograde interaction, and are differentiated by this property. The specifics of how these properties are initialised is described in Section 3.

Component	Parameter	Galaxies	
		Prograde	Retrograde
Halo	Mass [ $10^9 M_{\odot}$ ]	200	167
	Scale radius [kpc]	5.12	4.74
	Cut-off radius [kpc]	60.0	55.0
Gas disc	Mass [ $10^9 M_{\odot}$ ]	5.5	1.2
	Scale length [kpc]	2.18	0.93
	Cut-off length [kpc]	7.0	4.5
	Scale height [kpc]	0.18	0.15
	Cut-off height [kpc]	0.7	0.45
Stellar disc	Mass [ $10^9 M_{\odot}$ ]	4.57	2.57
	Scale length [kpc]	1.2	0.9
	Cut-off length [kpc]	3.6	2.7
	Scale height [kpc]	0.24	0.1
	Cut-off height [kpc]	0.72	0.27
Stellar bulge	Mass [ $10^9 M_{\odot}$ ]	4.0	2.28
	Scale radius [kpc]	0.2	0.1
	Cut-off radius [kpc]	0.35	0.13

### 3 NUMERICAL SIMULATIONS AND METHODS

In this section we outline the physical recipes for star formation and feedback, and describe our method for determining the initial properties and orbital parameters of the progenitor galaxies. The simulations presented in this work were performed with the hydrodynamics and  $N$ -body code RAMSES (Teyssier 2002), which uses an Adaptive Mesh Refinement (AMR) grid method with an HLLC Riemann solver (Toro et al. 1994). The code solves the conservative Euler equations for the dynamics of the gaseous component using a 2nd order Godunov scheme. We adopt an ideal mono-atomic gas with adiabatic index  $\gamma = 5/3$ . The Euler equations consider the hydrodynamics and the gravitational effects from stars, dark matter, and fluid self-gravity. Dark matter and stars only interact through gravity, as collisionless particles. We employ a sub-grid recipe for the formation of stars and their feedback, which we will describe briefly in the coming section and refer to Agertz et al. (2013, 2021) for details.

The aim of this study is to explore possible formation scenarios for the Haro 11 galaxy. To this end, we have performed roughly 500 low-resolution simulation tests of a merger between two disc galaxies, as part of an iterative trial-and-error parameter study to approach the orbital and galaxy parameters that agree with Haro 11 observations. To reduce the run time, no stellar feedback was included in the initial test simulations. For each simulation we varied various parameters relevant for the progenitor galaxy orbits (e.g. velocity) or their intrinsic properties (e.g. disc size) to make the simulation fit, by eye, with the morphology, SFR, kinematics, and stellar properties observed in Haro 11. Parameter changes that improved the model were kept and further iterated upon. However, there is no definitive best set of parameters as orbital and galactic parameters interact complexly, causing parametric degeneracies where significantly different sets of initial conditions can achieve similar results.

### 3.1 Star formation and feedback physics

In our simulations, the formation of stars is treated as stochastic events, with the amount of stars formed sampled from a discrete Poisson distribution and following the Schmidt law (Schmidt 1959; Kennicutt 1998)

$$\dot{\rho} = \epsilon_{\text{ff}} \frac{\rho_{\text{g}}}{t_{\text{ff}}} \text{ for } \rho_{\text{g}} > \rho_*, \quad (1)$$

where  $\rho_* = 100 \text{ cm}^{-3}$  is the density threshold for star formation,  $\rho_{\text{g}}$  is the gas density,  $t_{\text{ff}} = \sqrt{3\pi/32G\rho}$  is the free-fall time for a spherical cloud, and  $\epsilon_{\text{ff}}$  is the star formation efficiency per free-fall time. Star particles follow a Chabrier (2003) initial mass function with a total mass  $10^3 M_{\odot}$ . We adopt  $\epsilon_{\text{ff}} = 10\%$ , as this choice in galaxy simulations has been shown to reproduce the same low efficiency ( $\epsilon_{\text{ff}} \sim 1\%$ ) observed in giant molecular clouds (see e.g. Agertz & Kravtsov 2016; Grisdale et al. 2019, and references therein).

Stellar feedback follows the subgrid recipe detailed in Agertz et al. (2013, see also Agertz & Kravtsov 2015) and tracks the injection of momentum, energy, and metals of supernovae Type Ia, Type II, and stellar winds. Individual supernovae are considered resolved when the host cell is resolved by at least three cooling lengths, following Kim & Ostriker (2015), and is otherwise deposited in the neighbouring gas cells. Metallicity is traced through oxygen and iron, which are combined into a total metallicity according to the relative solar abundance (Asplund et al. 2009).

### 3.2 Fiducial progenitors setup

We based our initial guess of the galaxies' orbital parameters and inclination on the initial conditions of a simulation of the Antennae galaxies by Renaud et al. (2015). Ö15 made a comprehensive comparison between Haro 11 and the Antennae galaxies and found similarities between their morphology, kinematics, and stellar properties. Both galaxies are currently undergoing a merger, but with the Antennae galaxies being larger and more massive. The simulations by Renaud et al. manage to successfully recreate the morphology and several important properties of the Antennae. However, these galaxies have several observed differences between them and the initial conditions need to be tweaked to account for these.

Firstly, recent HI observations indicate that Haro 11 only has one visible tidal tail (Le Reste et al. 2024), compared to two in the Antennae galaxies. The strength of a tidal tail can be weakened by flipping the rotational axis (inclination) of one of the progenitor galaxies to form a retrograde orbital motion, but this does not guarantee that the tidal tail will be removed, as other properties interact in a complex way to affect its strength and shape. Notably, the Antennae galaxies are a symmetric interaction (in terms of mass, size, and morphology), while Haro 11 has been hypothesised to be the result of dissimilar progenitor galaxies (see the discussion in Section 2). For the initial setup we reduced the gas mass and size of the retrograde galaxy (as is detailed below), which is sufficient to reduce the strength of the tidal tail to be completely undetectable (see Section 5.1 for details on this process).

The Haro 11 galaxy is roughly one third the size of the Antennae galaxies, and we adopt this size scaling between our simulations and the Antennae simulation by Renaud et al. (2015). In their comparison, Ö15 indicate that the galaxy might be 4 times as dense as the antennae, which is apparent from the similar gas mass, but smaller size, between our prograde galaxy and NGC 4038 in the Antennae simulation. In Section 5.1, we show an example of how varying the size and density of the progenitor discs affects the final morphology.

**Table 2.** The orbital parameters and initial inclination of the two galaxies.

Galaxy	Position [kpc]			Velocities [ km s <sup>-1</sup> ]			inclination		
	$x$	$y$	$z$	$v_x$	$v_y$	$v_z$	$\hat{x}$	$\hat{y}$	$\hat{z}$
Prograde	+11.40	-32.77	+50.42	-8.94	-1.81	-15.72	+0.7138	-0.6680	-0.2105
Retrograde	-16.22	+32.88	-50.05	+8.94	+1.81	+15.72	-0.6710	+0.2138	+0.2048

### 3.2.1 Initial conditions

Both progenitor galaxies were modelled as disc galaxies with a NFW (Navarro et al. 1996) halo profile for the dark matter, a spherical Hernquist (1990) profile for the stellar bulge, and exponential profiles for the stellar and gas discs. The initial position and velocity of each particle and gas element was then generated by MAGI (Miki & Umemura 2018) using these profiles to distribute  $10^6$  dark matter particles,  $10^6$  stellar particles in the disc, and  $10^5$  particles for the stellar bulge. The gas disc was initialised as  $10^6$  particles, which were then deposited onto the AMR structure.

Table 1 lists the properties of each component in both progenitor galaxies, while Table 2 provides their orbital parameters and inclinations. The two progenitor galaxies are labelled *prograde* and *retrograde*, to differentiate based on which galaxy forms the tidal tail. The initial disc rotation velocities were calculated from each galaxy’s total mass profile and oriented according to their inclinations. The galaxies were positioned sufficiently distant to prevent any overlap between their respective halos, allowing a period of secular evolution before any significant tidal interaction.

In order to determine the initial mass budget, we assumed the galaxies have retained a mass baryon fraction  $f_b$  close to the cosmic baryon fraction  $\Omega_b$ , i.e.  $f_b = (M_g + M_*) / (M_g + M_* + M_{DM}) \approx 15.6\%$  (Planck Collaboration et al. 2020). We base the initial stellar mass on observational constraints and do abundance matching (following Figure 9 in Behroozi et al. 2019) to determine the mass of the dark matter halo. The total stellar mass of Haro 11 is on the order of a few  $10^{10} M_\odot$  (Östlin et al. 2001; Madden et al. 2013, ; Ö15). The resulting dark matter matches with the total dynamical mass  $\sim 10^{11} M_\odot$  of Haro 11, estimated by Ö15 through dynamical reasoning of velocity field observations in the outer part of the galaxy.

The initial gas mass of the galaxies was calculated as the total observed mass between the molecular, neutral, and ionised gas phase (see Section 2 for values). We then added  $1.25 \times 10^9 M_\odot$  to this mass, in order to offset the gas consumed through star formation during the simulation run (determined during test runs). Similarly, we removed the same amount of mass from the observed stellar mass to determine our initial stellar mass. Additionally, some of this gas mass budget is added to the circumgalactic medium (see below). The gas mass in the discs is added in the simulation as neutral gas, and any additional gas phases naturally form as the galaxy evolves. The initial metallicity of the gas discs was directly taken from observations ( $12 + [O/H] = 7.9$ , Ö15) and translated to a total metallicity  $Z = 0.2 Z_\odot$ .

The simulation was started at a low spatial resolution to allow the initial conditions to relax and then increased after a few 100 Myr, with plenty of time before the first interaction. The maximum spatial resolution of the fiducial simulation is  $\Delta x = 36$  pc, and is within a  $300^3$  kpc<sup>3</sup> volume. The circumgalactic medium spans the entire simulation volume with an initial temperature  $T \sim 10^8$  K and hydrogen number density  $n_H = 10^{-4}$  cm<sup>-3</sup>, which is within the densities observed of local galaxies and in simulations (Machado et al. 2018). A proper gas halo is necessary to produce realistic outflows and tidal tails, and to ensure the gas mass of the system matches

the cosmic baryon fraction for the given stellar mass. However, the circumgalactic gas content varies widely between systems and is not well constrained. We constructed a tests with higher and lower circumgalactic densities, which is briefly discussed in Section 5.4.

### 3.3 Strategy for tweaking initial conditions

This section details how the initial conditions for the two progenitor galaxies were improved upon through iteration. While our approach is similar to a parameter study, the focus of this project is to compare the fiducial Haro 11 model with observational data and discuss possible merger scenarios for the galaxy and its properties. We will not go into detail on the full range of parameters and their agreement with each observed property. Instead, we will here briefly discuss our approach for narrowing down the range of the parameter space, and in Section 5 we show visual examples of some early low-resolution tests. These tests demonstrate how some specific changes to the initial conditions affect the morphology of the resulting galaxy.

The main observed properties used for constraining our model were: gas and stellar morphology, SFR, gas kinematics, and stellar masses and ages. To match these, we varied for each progenitor galaxy these properties: positions, the velocities (speed and angle), gas/stellar mass content, inclination, and size of the individual galaxies. In particular, we explored the relative mass ratio and gas fraction between the galaxies, as these parameters are connected to the formation of tidal tails, and the gas fraction has been suggested to be different for the progenitors (see discussion in Section 2).

The orbit between the two galaxies is strongly entangled with all of the properties we want to compare with observations. Adjusting the velocity is the main control we have of the orbit, including the timing and proximity of the close interactions. The initial speeds were altered between half and twice the initial speed of the fiducial presented in Table 2. When evaluating the velocity angle we (primarily) changed the  $x$  and  $y$  velocity components, and with the aim to fine-tune the tidal tail and inner morphology.

Other than the velocity, the mass ratio between the galaxies has a large impact on the orbit. However, compared to the velocity the masses are not as easy to fine-tune and has additional effects on other observable. For example, the SFR depends on the orbit but the amount of stars formed in the individual galaxies depends on their halo properties in a non-linear way. Thus, the mass ratio was primarily changed in early tests.

The tidal tails were formed during the first encounter between the progenitors, which is closely connected to their initial orbit. Additionally, the inclination of each disc has a significant impact on the strength and morphology of the tidal tail (see discussion of prograde vs retrograde in Section 2). Further examples of how these parameters affect the appearance of the morphology are provided in Section 5.1. Additionally, the inner morphology of the galaxy is also dependent on these parameters, as well as the initial mass and size of the discs.

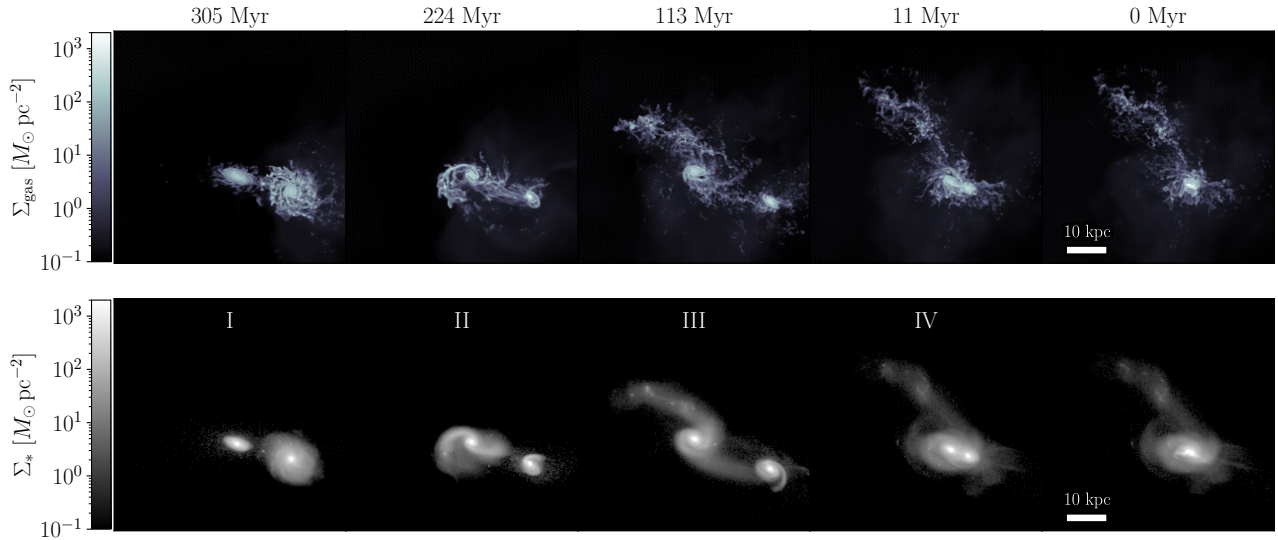


**Figure 2.** The column density of gas (top row) and stars (bottom row) for the large-scale structure of the galaxy are shown at various time outputs, spanning from the initial interaction to the point where the galaxy most closely resembles Haro 11. The plots marked with Roman numbering correspond to the times in the SFR plot in Figure 7.

### 3.4 Analysing the simulation output

The total runtime of the fiducial simulation is 1280 Myr, which is just after the centres of the two galaxies fully coalesce. We analyse the galaxy at the time output we deem to be closest in terms of SFR and morphology to the Haro 11 galaxy. This, current observed, time is set as 0 Myr and is as the galaxies are undergoing their second interaction. The morphology and kinematics we calculate are largely invariant on the choice of time by several Myr, but the SFR can vary by a factor of 2–4 within only a few Myr. After  $\gtrsim 10$  Myr, the morphology (and SFR) is notable different to Haro 11.

The exact morphology and kinematics of the inner galaxy is dependent on the viewing angle we adopt. Our approach is to find an angle by eye that improves the match for the inner morphology (i.e. relative position between knots and the ‘ear’) while keeping the tidal tail at roughly the correct relative angle to the inner morphology. The fiducial viewing angle is in-between the  $z$  and  $y$  axis of the simulation (specifically,  $\hat{n} = [0.26, -0.64, 0.72]$ ). The morphology is insensitive to a change in angles within a subtended angle  $\sim 10^\circ \times 10^\circ$ , with some directions being less or more affected.

The SFR is calculated by binning stars by stellar age, summing the stellar mass within each time bin, then subtracting the stellar mass of a neighbouring bin and dividing by the bin size. Our results are presented with a 1 Myr bin width to highlight the quick variations during the interactions. However, if adopting 10 Myr bins, which is equivalent to the timescale for H $\alpha$  observations, the overall SFR history was found to be similar.

## 4 THE FIDUCIAL HARO 11 MODEL

In this section we present our fiducial Haro 11 model, chosen from among a large set of simulations (following the method in Section 3.2) as one of the best matches by eye with various key features of Haro 11. In particular, we compare the morphology (inner and tidal tail), SFR, stellar properties, and kinematics in our simulation with observational data. This simulation setup offers a broad agreement between

**Table 3.** Properties of the galaxy from the fiducial Haro 11 simulation, analysed at current time, when the morphology and SFR best match observations, for a volume of  $60 \times 60 \times 60 \text{ kpc}^3$  around the central part of the galaxy. We separate between ionised gas around the galaxy ( $< 10 \text{ kpc}$ ) and ionised CGM gas, as the latter has no observational comparison. The CGM is, thus, excluded from the gas fraction and total gas mass.

Stellar mass [ $10^9 M_\odot$ ]	16.49
Total gas mass [ $10^9 M_\odot$ ]	4.33
Gas fraction [%]	20
Molecular gas mass [ $10^9 M_\odot$ ]	1.35
Neutral gas mass [ $10^9 M_\odot$ ]	1.06
Ionised gas mass [ $10^9 M_\odot$ ]	1.77
Ionised CGM gas mass [ $10^9 M_\odot$ ]	1.90
SFR [ $M_\odot \text{ yr}^{-1}$ ]	43

all these different properties, which indicates it serves as a good basis to describe the formation scenario of Haro 11. We discuss the strengths of our fiducial model as the origin of Haro 11 and apply it to interpret observations in Section 6, along with discussing possible improvements for future numerical work.

Additionally, we present the current stellar and gas masses, as well as the SFR, of this simulation in Table 3. The gas mass is also divided into phases by weighing the mass by phase-specific variables, such as H $\alpha$  emissivity (see Ejdetjärn et al. 2022, for details): molecular, neutral, and ionised, in order to compare its distribution with observations. However, we note that the gas phase masses are uncertain, as they are sensitive to the stellar formation and feedback recipes adopted. Additionally, ( $\sim 1.9 \times 10^9 M_\odot$ ) of hot/warm ionised gas within the halo of our galaxies, which is too diffuse to be observed and therefore not added to the ionised gas mass budget.

### 4.1 Tidal tail

The first step of analysing the simulation is to visualise the merger process and the tidal tail, as it is one of the strongest signs of Haro

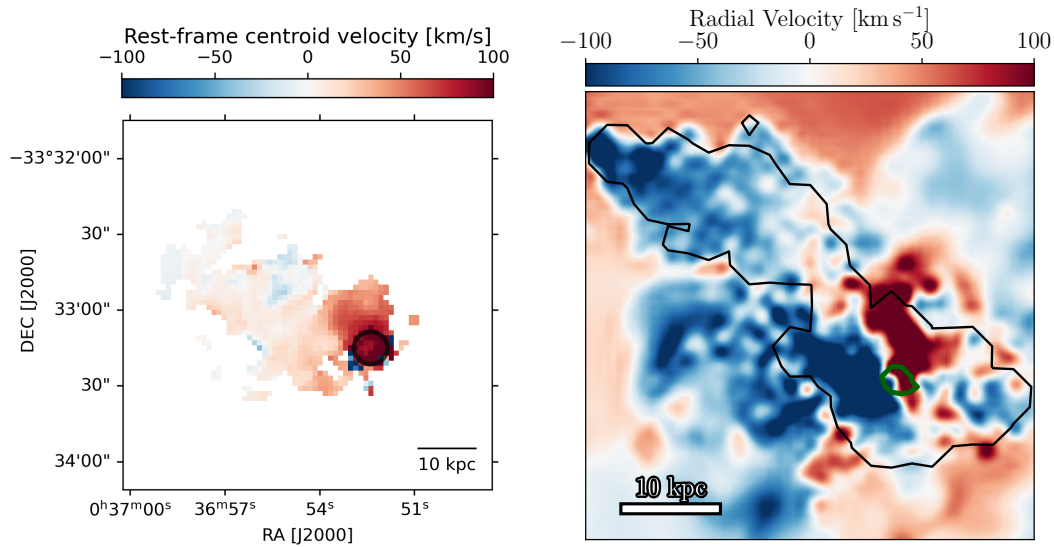


**Figure 3.** Velocity maps of the HI tidal tail. Left plot shows the 21-cm line, in emission only, of Haro 11 with MEERKAT (Le Reste et al. 2024, see their paper specifics of the observation and data reduction). The systemic velocity of the observation is  $\sim 6190 \text{ km s}^{-1}$ . Right plot shows the simulation; the green contour outlines the central stellar component, and the black contour outlines the gas column density exceeds 10% of its maximum value.

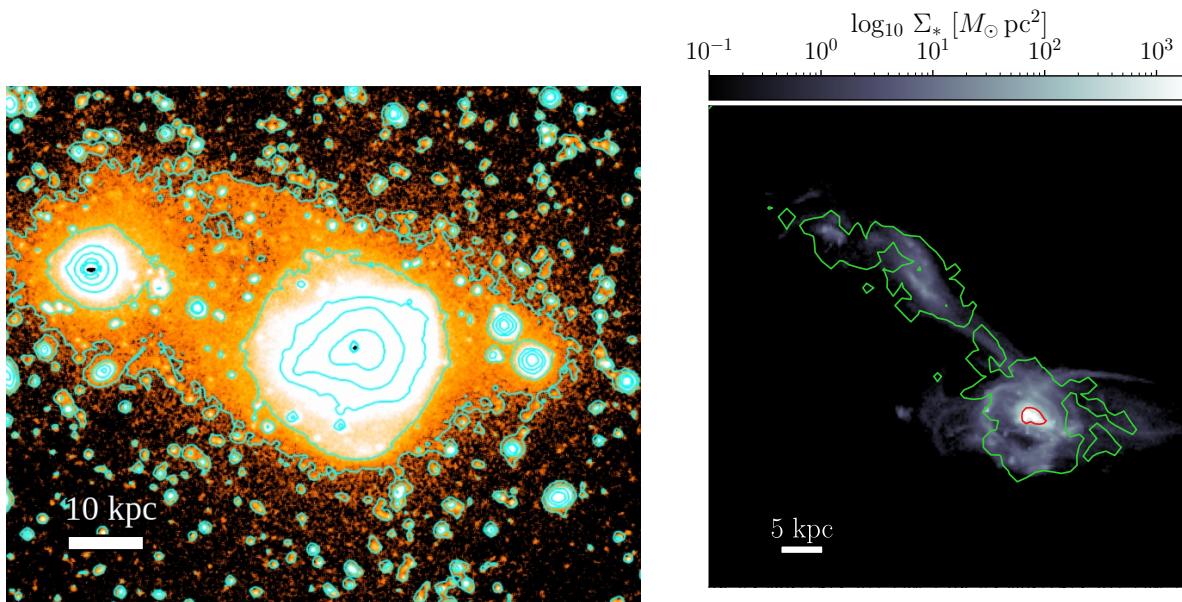


**Figure 4.** The stellar tidal tail from observations (*left*) and simulations (*right*). The simulation has green contours showing the gas distribution and the red contour highlights the inner region. The observations are in the B-band with VLT/FORS (see details in Section 4.1), with green contours showing the stellar distribution.

11 being a merger. In Figure 2 we present several projection maps of the gas and stars as part of a timeline of the simulation. These maps follow the formation of the tidal tail, from the first close interaction until they reach the current observed time of Haro 11, which is  $\sim 10 \text{ Myr}$  into the 2nd interaction; a time period of roughly  $\sim 200 \text{ Myr}$ . Furthermore, the maps have Roman numerals annotated, corresponding to time markers in the figure of SFR as a function of time in Section 4.3, which highlights the burst of star formation during the close interactions.

This simulation matches the length and kinematics of the HI tail presented in Le Reste et al. (2024) using MEERKAT observations

of the 21-cm line<sup>1</sup>. The tidal tail is extending in the same direction relative to the inner morphology as in Haro 11 (north-east) and have the same length  $\sim 40 \text{ kpc}$ . Furthermore, we find that the relative HI mass inside the tidal tail is  $\sim 36 \%$ , which is within the observed value  $44^{+20}_{-19} \%$ . A velocity field map of the HI in emission only are presented in the left plot of Figure 3, and the HI velocity in our simulation is on the right. The HI tail is blue-shifted at a speed

<sup>1</sup> The reduced MEERKAT 21 cm data is publicly available at: <https://archive-gw-1.kat.ac.za/public/repository/10.48479/7zn6-bw59/index.html>

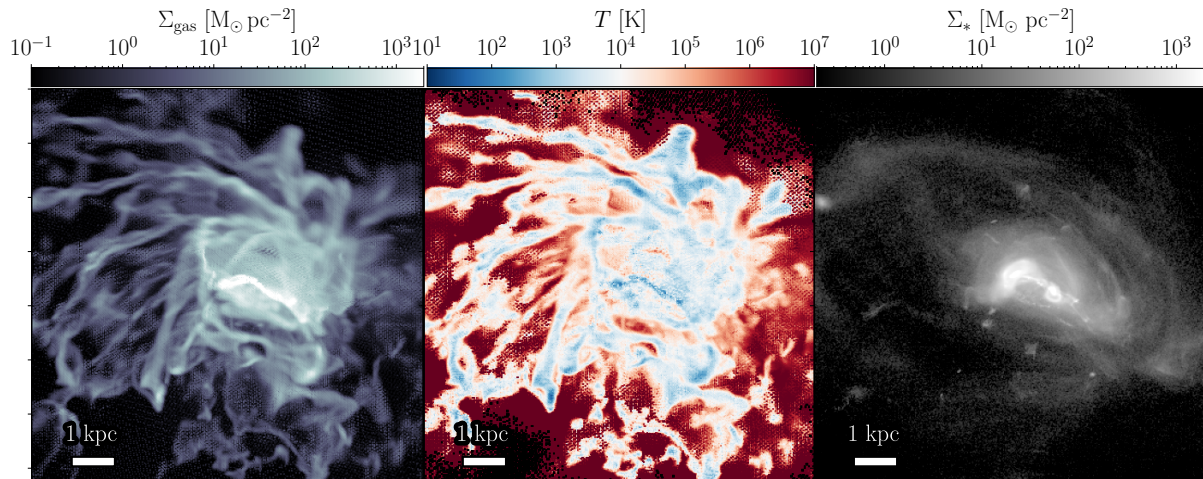


**Figure 5.** Projections maps of the inner part of the galaxy at the output where the galaxy most closely resembles Haro 11.

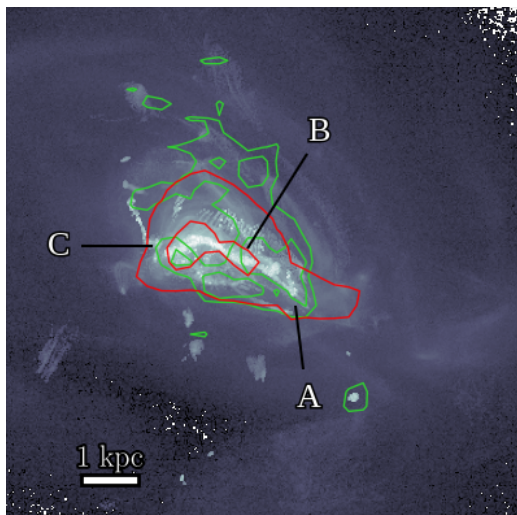


**Figure 6.** Projection map of the stellar mass weighted by their inverse stellar age,  $M_* = M_* \times (t/4 \text{ Myr})^{-1.25}$ , to represent young, bright stars. The red/green contours correspond to the projected stellar/gas column density. Combined with Figure 1, in which knot A is not readily observed due to this extinction, this map demonstrates that bright stars form in knot A but are obscured by dust.

$\sim +50 \text{ km s}^{-1}$ , which is slightly slower compared to our simulations with a mean velocity of  $\sim +80 \text{ km s}^{-1}$ . The same map, but for the absorption, is presented in Appendix A.

We next present the detection of a stellar tidal tail in Haro 11, the first to confirm the existence of a stellar component to the tidal tail. The observation was made in the B-band with VLT/FORS for a net integration time of 6240 s and reduced in a standard manner<sup>2</sup>. The image is presented on the left plot in Figure 4, along with an image of the stars in our simulations on the right. Furthermore, there is a much shorter, parallel component, to the tail and a short feature extending

<sup>2</sup> Applying bias subtraction, cosmic ray removal, flat fielding and atmospheric extinction correction.

to the upper right (NW). The latter two features are contaminated by the extended PSFs from bright stars, but are real. In addition, an archival HST/WFC3/IR/F160W image confirms the existence of these features at low S/N but the field of view is too small to fully map the Haro11 tidal system. The morphology of the tidal tail agrees with our simulation, but also the small feature extending in the upper right from Haro 11 can be found in our fiducial galaxy.

The stellar tidal tail is slightly shorter than the HI component ( $\sim 30 \text{ kpc}$  compared to  $\sim 40 \text{ kpc}$ ). This is likely due to a difference in scale radius or truncation between the two components, i.e. the gas disc extending further. We briefly explored the effects of truncation on the disc in Section 5.1. Additionally, the image of the stellar tidal tail shows clear shell structures around the galaxy. The simulation shows signs of these shells as well, which is encouraging for our model but is not useful as a constraint.

#### 4.2 Inner morphology

In order to put our simulations into context, we first present an observations of the Haro 11 galaxy on the left in Figure 1. This was presented in Adamo et al. (2010) using HST in three wavebands filters; in particular they use 220W and 814W with the ACS/HRC instrument, and 435W with ACS/WFC. Additionally, the right plot of the figure shows a mock observation of our simulation using the post-processing radiative transfer code RASCAS (Michel-Dansac et al. 2020) to obtain the stellar continuum and apply the same HST filter profiles as the observations. The key morphological features of Haro 11 are annotated: three distinct stellar knots (A, B, C) and a dusty arm going upwards from knot A to the right of knot B (the ‘ear’). All of these morphological features can be identified in the mock observation as well, but knot A is not as readily apparent, which is discussed below.

The inner gas and stellar morphology, as well as temperature, of the galaxy at the current observed time is presented as projection maps in Figure 5. The high density gas around knot B and A correspond to areas of high stellar density. The disc arm with young stars is seen in the right-side of the plots is reminiscent of the ear observed in Haro 11. Compared to observations, the positions of these features are slightly mismatched in position relative to each other, but are

broadly in the expected positions. Additionally, the dense gas that is overlapping with the stellar core on the left (knot C) is behind the core.

The main reason that knot A is not observed in our mock observations is due to the dusty arm covering the stars, but we can infer its presence from the stellar mass and young population. In Figure 6 we show a stellar map weighted by the inverse stellar age, as  $M_* = M_* \times (t/4 \text{ Myr})^{-1.25}$ , which is an approximate bolometric luminosity weighting; this highlights the presence of young, luminous stars. This figure shows that there is significant mass of young stars around knot A, which would be visible in the absence of extinction. Additionally, in Figure 8 we present a projection map of the median stellar ages, from which it is also evident that all of the knots, including A, contain many young stars. From this, we surmise that knot A likely reside within the disc arm (which also makes up the ear) of the prograde progenitor galaxy, which has its centre at knot B.

### 4.3 Star formation rate

Observations show that Haro 11 is currently experiencing a burst of star formation, which is attributed to an undergoing merger. We present the SFR as a function of time in Figure 7, annotated with Roman numbers as timestamps to the timeline images in Figure 2 and with shaded areas for the time of pericentre passages. The figure shows two peaks in the SFR that are associated with close interaction between the two galaxies. The SFR burst is thus likely caused by interaction effects, e.g. gas compression due to tidal forces, cloud-on-cloud collision, tidal torques that drive gas towards the centres of the galaxies (e.g. [Renaud et al. 2014b, 2019](#)).

The current day SFR from observations match with the observed values of our fiducial simulation. Furthermore, the starburst periods in our simulations can be readily compared to observations of stellar populations with distinct ages, which helps constrain the star formation history. The peaks indicate that these stellar populations should have ages of roughly 200 – 250 Myr, from the first interaction, and a few Myr, from the current interaction. We will explore this further in the next section by comparing stellar analysis models of the populations in the three knots.

### 4.4 Knot properties

We next evaluate the age and mass of the stellar knots. The knots are identified as shown in Figure 1, around a 0.5 kpc radius (1 kpc for knot A as it is less concentrated than the other knots). We want to compare with the stellar masses and ages of individual knots attained by [Sirressi et al. \(2022\)](#) from their SED fitting. To this end, we divide the clusters into three populations of age ranges: 1-4 Myr, 4-40 Myr, and 40-300 Myr, which is comparable to the populations in their best fit (we extend the range to 300 Myr to account for uncertainties in the precise time of the first interaction). For clarification, we will not present any detailed quantitative comparison of the stellar masses inside the knots, as the observational uncertainties reported allow a wide range of ages and masses, and the exact mass in our simulations depend on, e.g., the specifics of the model and observed time.

We begin by noting that knot B and C contain a significant amount of old  $\geq 100$  Myr stellar mass, on the order of  $\sim 10^8 M_\odot$ , while in knot A this mass is an order of magnitude lower  $\sim 10^7 M_\odot$ . Also, the average age of stars in knot A and B are much younger than those in knot C. All these features are in agreement with properties of the three knots reported by [Sirressi et al. \(2022\)](#). Furthermore, Figure 8 details the median stellar age distribution for the knots, and outlines

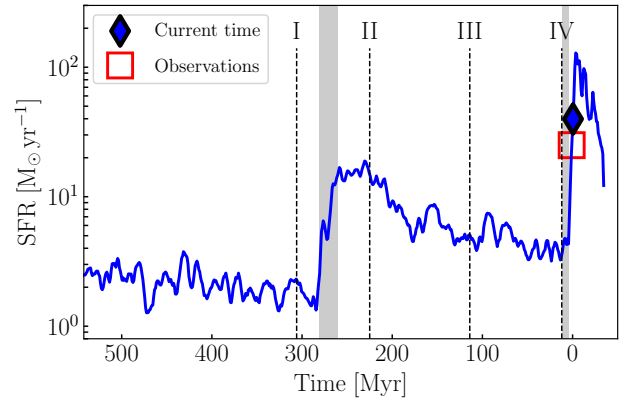


**Figure 7.** The star formation rate of the simulation. The time axis is set that the current observed time is at 0 Myr. Only the last  $\sim 500$  Myr are shown, as there is no interaction between galaxies before this and the galaxies have reached a roughly constant SFR (see Section 3.4 for details). Specific time periods are marked with Roman numbers, corresponding to the projection maps with same number in Figure 2. The grey shaded areas are the estimate pericentre periods of interaction. The starbursts at 0 Myr and 250 Myr correspond to close, gravitational interactions. The diamond marks the time at which the galaxy best resembles Haro 11, following the criteria in Section 3.2, and the square represent the SFR range mentioned in Section 2. The galaxy is in the middle of its second starburst event, with a SFR =  $43 M_\odot \text{ yr}^{-1}$ .

the various features in the galaxy along with a contour of the stellar mass distribution. Knot B and C are a mix of old and young stars and have a median age of  $\sim 150$  Myr, while knot A is primarily young stars. Additionally, the regions between the knots are forming new young stars.

We briefly explore the cluster mass and age distribution in the knots. To identify clustering within our simulations, we employ the friends-of-friends algorithm HOP ([Eisenstein & Hut 1998](#)) on a 12 kpc box around the galaxy centre (roughly corresponding to stars observed in e.g. Figure 5). A cluster is defined as having stellar peak densities  $50 M_\odot \text{ pc}^{-3}$ , a minimum density to merge groups as  $50 M_\odot \text{ pc}^{-3}$ , and outer density threshold of  $0.1 M_\odot \text{ pc}^{-3}$ ; set at a low value to detect the spread out clusters in knot A. We identify roughly 600 clusters, which is a large amount of clusters for a smaller galaxy. This is primarily due to the lower peaks and thresholds we set; higher thresholds for the stellar peak and minimum density ( $100 M_\odot \text{ pc}^{-3}$ ) resulted in a few hundred clusters. This choice did not affect our conclusions, but helped to identify more of the clusters in knot A.

The distribution of mass and median ages of the clusters, divided into their knot affiliation, are presented in Figure 9. As mentioned in Section 4.3, we notice two massive populations of star clusters that form during the starburst peaks that coincide with the close interactions. These groups of population ages,  $\sim 10^6$  Myr and  $\sim 10^8$  Myr, have been found in stellar population synthesis models of Haro 11 ([Chandar et al. 2023; Papaderos & Östlin 2023](#)). We recover in the simulation star clusters as massive as those found in the observations at the youngest age, while the majority of the old population would remain undetected at masses below a few times  $10^5 M_\odot$ ; as can be seen from the 90% completeness limit from [Sirressi et al. \(2022\)](#), presented as a dark line. The most massive clusters found in our simulations  $\sim 10^8 M_\odot$  are not found in the observations, but could stem from insufficient mass resolution, the cluster identification, or other, more spurious, effects. We plan to, in [Ejdetjärn et al. \(in prep\)](#), perform more extensive analysis of the cluster formation within our high-resolution simulations of the same setup.

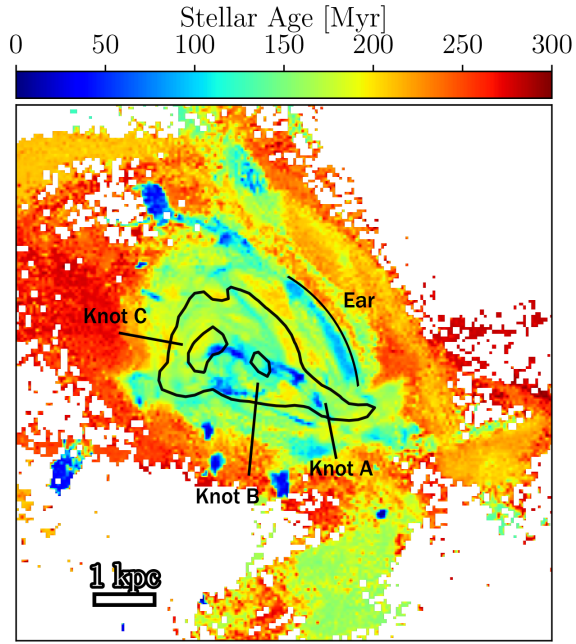


**Figure 8.** Projection map of the median stellar ages with black contours of the stellar column density. Labels and lines mark the various features described in Figure 1.

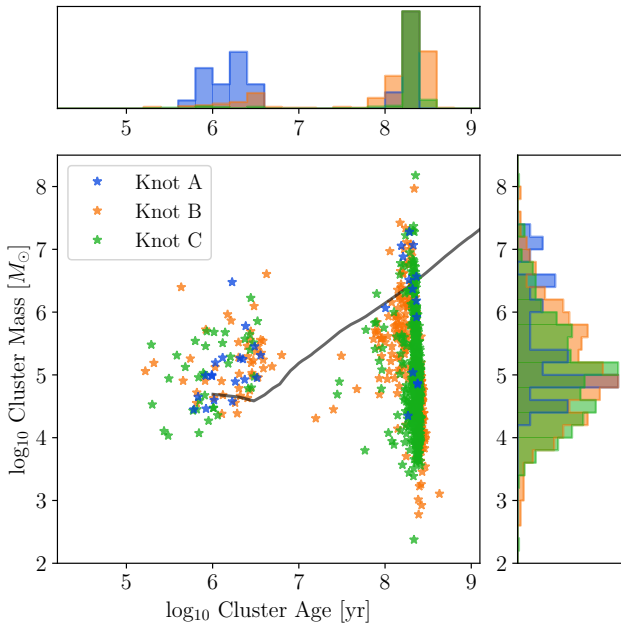


**Figure 9.** Distribution of masses and ages of the stellar clusters in the three knots, calculated as described in Section 4.4. The heights of the histograms are normalised to the same maximum height. The black line shows the 90% completeness of the stellar populations in Sirressi et al. (2022).

#### 4.5 Kinematics

In this section we present the gas kinematics of the inner galaxy, while the tidal tail kinematics are presented in Section 4.1. We produce mock observations of the  $H\alpha$  velocity field, in order to compare with the  $H\alpha$  observations from Menacho et al. (2021). Velocity maps from their observations and our simulation are presented in the left and right plots, respectively, in Figure 10. The mock  $H\alpha$  velocity was calculated as the weighted-mean of velocities, using  $H\alpha$  emissivities (calculated following Ejdetjärn et al. 2022, 2024) as weights. Additionally, the gas and stellar distribution is annotated as black and white contours, respectively.

The velocity maps show a broad likeness, with the gas being blue-shifted on the left side of the galaxy and the red-shifted on the right side. Additionally, knots A and B are within the gas moving towards us, this kinematic likely originates from the disc arm on this side. Knot C is located between a region of blue- and red-shifted gas, which also agrees with our simulation. However, there is a discrepancy between the magnitude of the velocity maps, as our simulations have about twice the speed of the observations. We discuss possible origins and solutions to this mismatch in Section 6.

The observations by Menacho et al. (2021) show channels of ionised gas cones, which they identify as outflows from stellar feedback. However, it is not within the scope of this paper to disentangle outflows from the  $H\alpha$  velocity field in our simulation, as it would not provide a reliable comparison; the  $H\alpha$  velocity field is sensitive to the specifics of stellar formation and feedback recipes, as well as the stochastic nature of feedback.

In Ö15, the authors made a comparison between the position-velocity (PV) diagram of the Antennae galaxies and Haro 11, which they noted had a similar shape and velocity magnitude. They acquired data using the CIGALE instrument and archived data for the Antennae. Their data covered a straight line going from knot C to A, and extending a few kpc beyond them. We follow their method and present our own PV diagram in Figure 11. The  $x$ -axis is determined as the projected distance along the dark line on the left plot in Figure 10. The left/right plot in the figure shows the simulation/observational data, which have very similar shapes with peaks and valleys at roughly the same distance intervals. We highlight these similarities, with a broad grey line in both plots, which is the mean velocity of the simulation at each distance in bins of 0.5 kpc. This figure also highlights that several of the simulation cells attain much higher speeds, as much as twice as fast, as the observations. However, the mean velocity (grey line) follows the same sine-like shape and are within the limits of the observational data.

#### 5 ADDITIONAL TESTS AND THE IMPACT OF SPECIFIC PARAMETER VARIATIONS

We next summarise the impact of some specific parameter changes on the resulting properties of our fiducial Haro 11 model. In particular, the compared properties in the previous section: morphology, star formation, and kinematics. To summarise, we find that these properties are stable to minor variations in individual parameters but the exact morphology and SFR is dependent on the complex interplay between several parameters. Additionally, the parameters that have the most significant impact are those that alter the orbit, e.g. mass ratio and initial velocity.

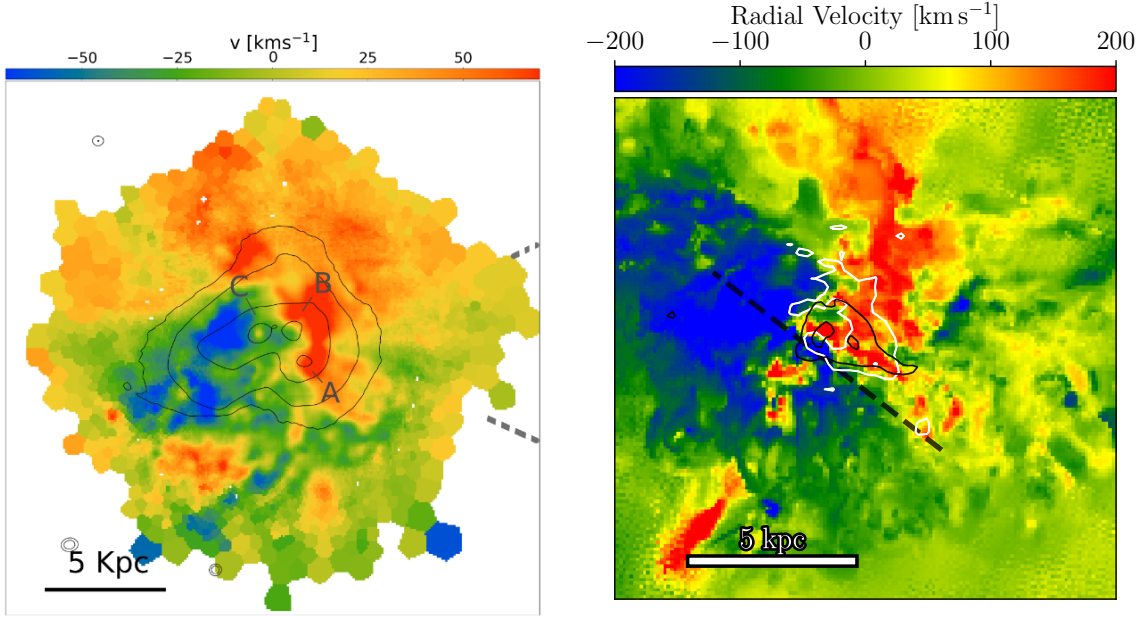


**Figure 10.** The  $H\alpha$  velocity field of observations in Menacho et al. (2021) (left; their Figure 2) and our simulation (right). The simulation shows contours of the stellar (black contours) and total gas (white contours) annotated. The black dashed line is used for the analysis of Figure 11. Note that the scale of the velocity magnitude in the simulations is roughly twice as large as the observations.

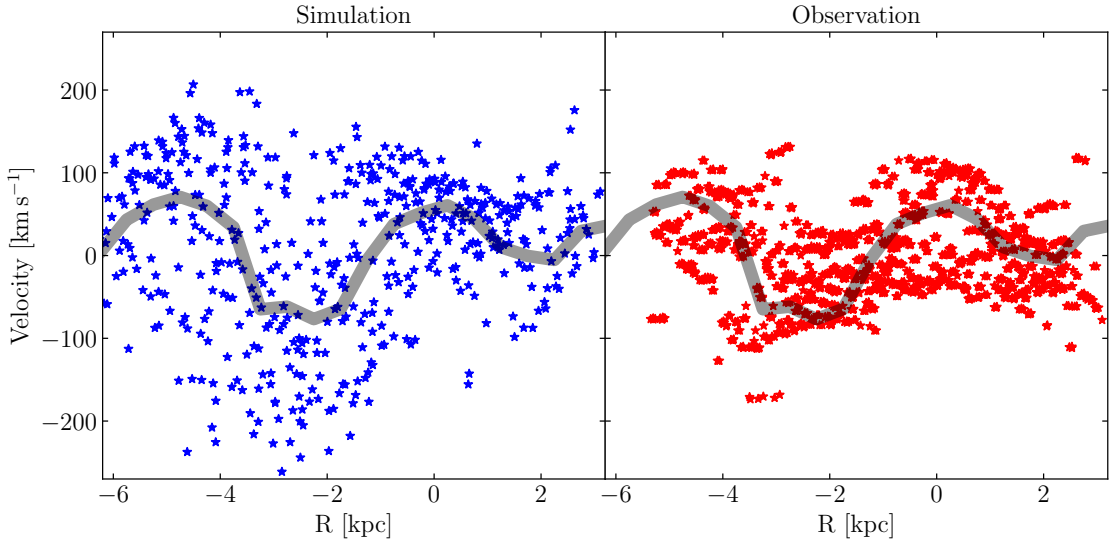


**Figure 11.** The PV diagram of our simulations (left) and observational data (right) of Haro 11. The  $x$ -axis corresponds to the projected length along the black line in Figure 10. The observational data was reproduced from Ö15, which they obtained using the CIGALE instrument. The grey curve in both plots is the weighted-mean of the simulation data in distance bins of 0.5 kpc. See Section 4.5 for details on how these plots were made.

### 5.1 Producing one tidal tail

In the previous section we demonstrated that our fiducial simulation is able to reproduce the *one* tidal tail, as observed in Haro 11, along with some of its features. However, producing a single tidal tail in this setup is non-trivial and requires a certain combination of parameters. In particular, in the top row of Figure 12 we illustrate that one of the galaxies need to have a retrograde orbit *and* the merger needs to be asymmetric (difference in mass ratio and/or gas fraction) to fully suppress the retrograde tail. The figure shows three projection maps of the gas density that, from left to right, highlight the decrease in

tidal tail strength: from prograde and retrograde galaxies (left), to a smaller and less massive retrograde disc (middle), to larger mass ratio difference between the galaxies (right). Additionally, it can be surmised from the rightmost image that the mass ratio also affects the strength of the tidal tail from the prograde galaxy, as a lower mass companion galaxy is less efficient at stripping gas.

Additionally, truncating the gas disc also has an effect on the resulting morphology of the tidal tails. In the centre row of Figure 12 we show an initial galaxy with retrograde and prograde motions (left), a thicker disc for the retrograde (middle), and a truncated disc

for the retrograde (right). The thicker disc can be seen to yield a slightly weaker 2nd tail and have more tidal features surrounding it. The truncated disc also shows a more diffuse 2nd tail and possibly some small changes to the main tail.

From our simulation tests, we learned that the length of the tidal tail puts a constraint on the time since the first interaction, when the tail first forms. In order for the gas tail to reach the observed 40 kpc, it would need roughly 200 Myr to expand. For comparison, a shorter interaction time of  $\sim 100$  Myr would yield a length of  $\sim 20$  kpc. This time might be a lower limit, as the observed expansion speed of tidal tail is slightly lower in the HI observations. Furthermore, the presence of a tidal tail this long also substantiates that Haro 11 is at least in its 2nd close interaction.

## 5.2 Varying velocity

We briefly overview the effects of varying the initial velocities, as velocity is connected to characteristics of the tidal tail and the stellar populations (the interaction times are connected to the SFR bursts). Generally, increasing the speed of the progenitors extended the time before the second encounter, giving the tidal tail more time to extend further. However, it also leads to a very brief interaction time which results in a weak tidal tail. In contrast, lower velocities lead to a quicker merger and shorter tidal tail, but the gas within the tail is denser.

In the bottom row of Figure 12, we visualise the impact of changes in speed and angle. The leftmost image shows a prograde and retrograde galaxy at a 1.2 times speed of the fiducial tests (see left plot in centre row for comparison) and the middle image is at a 0.8 times the speed. The right image shows a more direct impact angle, resulting in more gas debris and a shorter interaction time. As an aside, the simulation with lower initial speed did not seem to result in any significant change in the magnitude of the velocity field.

## 5.3 Elliptical vs disc

A formation scenario proposed mentioned in Adamo et al. (2010) is that the progenitor galaxies of Haro 11 could be a low-mass, evolved galaxy and a gas rich (disc) galaxy, due to the irregular gas morphology around the knots and stellar age distribution (see discussion in Section 2). We briefly explored a setup where the retrograde disc was replaced by a gas-poor, dwarf elliptical galaxy. For this test, we kept the total mass of the systems the same, but the gas and stars was re-distributed between the galaxies to replace the prograde disc with a sphere<sup>3</sup> of stars with no gas. An image of the tidal tail gas density is presented in Figure 13, which shows that this approach also exhibits only one tidal tail; as to be expected when there is no disc material to be stripped. Additionally, the extended spherical shape cause some additional tidal substructures to appear. We did not analyse the inner morphology.

The SFR of this scenario is lower leading up to the first encounter, after which it is comparable to other test simulations with discs. Although, it does not reach the same peak in SFR nor exhibit any distinct bump during the first encounter, compared to the fiducial simulation in Figure 7. This does not necessarily eliminate this specific merger scenario, as other changes, such as a higher gas fraction in the prograde galaxy, could be made to boost the SFR.

<sup>3</sup> The stellar distribution followed a Hernquist profile with similar scale radius as the original disc.

## 5.4 Density of the CGM

Additionally, we performed a few tests varying the circumgalactic density. The fiducial value  $\rho_{\text{CGM}} = 10^{-4} \text{ m}_{\text{H}} \text{ cm}^{-3}$  is calculated by spreading some of the gas mass in a  $60^3 \text{ kpc}^3$  cube, i.e. the size of the largest of the two dark matter halos. This gas mass was taken as the baryonic mass missing from the galaxy mass to reach the cosmic baryon fraction. In Figure 14 we show an example of how the increased density affects the tidal tail structure. The tail can be seen to go from being one coherent structure at low density and becomes clumpy towards higher density. Comparably, observations of the HI tail show that the tail is clumpy in nature (Le Reste et al. 2024), which could be due to interactions with a dens halo of gas or clumpiness within disc before or during stripping. Notably, a more gaseous halo would also affect the shock structure of ejected gas and could be compared with observed ionisation structures, but due to these examples having no stellar feedback there is no evident difference in outflow shocks.

## 6 DISCUSSION

### 6.1 Caveats and alternative merger scenarios

We have in the previous sections demonstrated that our simulation setup of two disc galaxies undergoing a merger is able to reproduce the key features of the morphology, kinematics, SFR, and stellar population of Haro 11. Finding a model that is able to reproduce several different features of a specific galaxy is not trivial and is encouraging for the reliability of the presented merger scenario. However, there are caveats to our results: the model is not accurate enough for detailed comparison and there are degeneracies between different setups. Here, we connect back to the observational data to address the strength and weaknesses of our simulation model.

The simulations in this work show that the presence of a tidal tail, as reported by Le Reste et al. (2024), are in agreement with the scenario that Haro 11 is currently undergoing a merger. This is further confirmed by new observational data presented in this work of a stellar tidal tail, which is the first time the stellar component has been captured. However, because the Haro 11 tidal tail is observed as a 2D projection and does not show any curvature or other distinct morphological features, it is difficult to model the tidal tail morphology in detail, which limits the constraint to the length and width of the tail. This puts more emphasis on also matching the kinematics and other properties, such as the relative HI gas fraction. We find that the properties of the observed tail match with our fiducial Haro 11 simulation, and since the properties of the tidal tail are closely connected to the orbital conditions, this is a good indication that the orbit of the fiducial simulation are correct. Another sign of this is our discovery that a specific set of parameters are required for the second tidal tail to be undetectable.

The inner morphology of Haro 11 has a few distinct features that we are able to match: the three stellar knots, the disc arm of gas and stars ('ear'), the 'bent' shape of the galaxy, in particular knot A and B being covered by gas. Fitting the exact positions of the knots (relative each other) and the orientation of the disc arm requires detailed tweaking of orbital parameters. Additionally, the relative position of the knots is closely connected to the viewing angle and the chosen time output. We note that by varying these, the position of these morphological features can be improved. However, changing the angles was found to lead to a severely worse match with other features; primarily the length, position, and kinematics of the tidal tail.

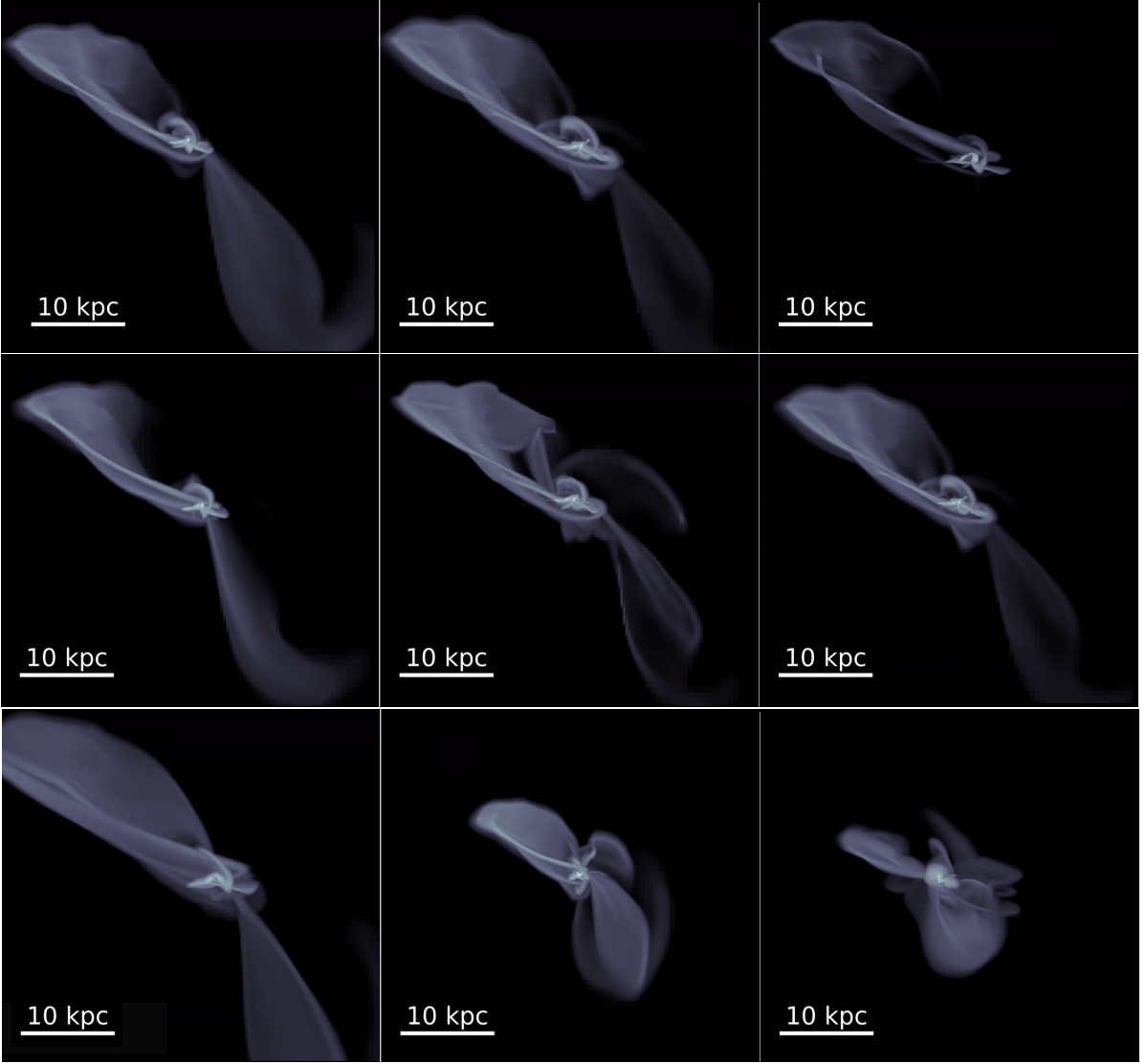


**Figure 12.** Projection maps of the gas densities, with each row showing the impact of specific parameters. *Top:* Highlights the successive removal of the second tidal tail, from left to right. Left: one prograde and one retrograde galaxy. Middle: reducing the gas mass and size of the retrograde galaxy. Right: changing the mass ratio between the two galaxies, by reducing the dark matter mass of the retrograde galaxy. *Centre:* Highlights the morphological impact of disc size. Left: One galaxy has retrograde motion and the other has prograde. Middle: Thicker disc for the retrograde. Right: Truncating the gas and stellar disc at 2/3 the original radius. *Bottom:* Highlights the morphological impact of the initial velocity. Left: The original Antennae initial conditions (scaled down in size), see Section 3.2 for details. Middle: Slower initial speed, causing a shorter merger time and more direct impact. Right: A more direct impact between the galaxies, which forms more debris.

Furthermore, we have shown that knot B and C are the centres of the progenitor galaxies while knot A is part of the stellar disc around knot B, which is in agreement with observations of the morphology (knot B and C being more compact than knot A) and the relative mass between the knots. Currently, the galaxies have had a close interaction and are moving past each other, reaching their apocenter a few Myr later into the merger. Just a few Myr after this, the prograde galaxy’s bulge will be closer to where knot A is expected and in knot B’s stead a very young stellar population will form from the intense gas compression between the galaxies. Thus, the morphology of the galaxy shifts sharply during the merger, which presents an alternative merger scenario where knot B is not a core but mainly composed of young stars. However, this alternative scenario is unlikely based on the knot’s observed compactness and stellar ages.

From our mock observations in Figure 1, knot A is not evidently

visible. This is likely due to the amount of dust and gas within the arm, obscuring the knot. Instead, we infer its presence from the stellar mass distribution, young stellar ages, and the placement of the disc arm. Additionally, the amount of young stars in knot A could affect its visibility. This depends on the specifics of small-scale physics such as the star formation efficiency and gas clumping, but also the gas fractions and timing of observations.

The final gas and stellar mass between simulation and observations are in agreement, but this is neither surprising nor a viable constraint as the galaxy are modelled to have similar masses. However, it is reassuring that no additional effects, such as stellar feedback and tidal stripping, have significantly altered this match. Furthermore, the comparison between gas phases is uncertain, but it is encouraging that there is a broad agreement in the distribution. Although, there is a significant amount ( $1.90 \times 10^9 M_{\odot}$ ) of hot/warm ionised gas

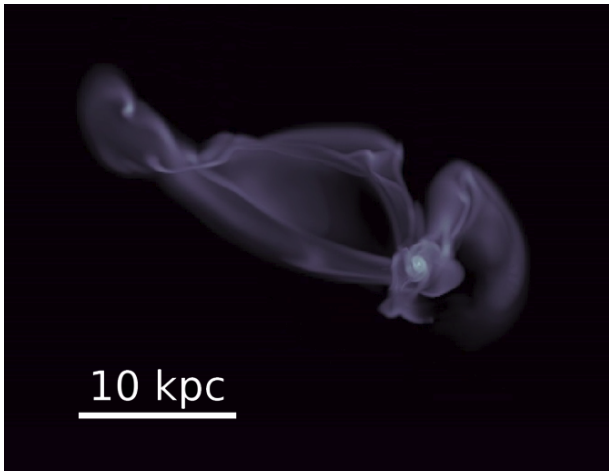


**Figure 13.** Projection map of the gas density in a setup with an elliptical galaxy and a prograde galaxy.

within the halo of our galaxies, which is too diffuse to be observed and therefore presented separately from the ionised gas mass.

The velocity field is one of the most challenging components to utilise as a comparison with our simulations, as the velocities are highly sensitive to numerous factors, e.g. the orbits, rotational velocity, stellar feedback, and viewing angle. Primarily, it serves to confirm the general kinematics resulting from the orbital parameters, rather than providing precise constraints. To this end, our simulation matches the general appearance of the observed velocity field. However, the inner  $H\alpha$  velocity show speeds around twice the magnitude of observations, which indicates that the initial orbit or disc rotation should be slowed down. The issue with reducing the orbital speed is that the length and velocity of the tidal tail is sensitive to this parameter, and would decrease its length while also cause more gas to be stripped (making the second tail more visible). Thus, a change in the orbit or disc properties appears as the more likely solution, but would require extensive exploration of a different parameters space.

The SFR of our chosen output is slightly higher than the observed SFR ( $\sim 40 M_{\odot} \text{ yr}^{-1}$  compared to  $\lesssim 30 M_{\odot} \text{ yr}^{-1}$ ). This increases to  $\gtrsim 100 M_{\odot} \text{ yr}^{-1}$  within the time it takes the galaxies to merge and the morphology to become unrecognisable. Even if we chose this later output, the factor of two difference in the SFR is well within the uncertainties of small-scale physics within the simulation that regulate star formation, e.g. the adopted star formation efficiency, stellar feedback, among other factors. We found that the SFR was stable to small tweaks to the orbit, with exception of close interactions. However, the SFR is highly sensitive to the chosen time output we choose to observe, due to the fact that the Haro 11 model is currently undergoing a powerful starburst which can vary from a few  $M_{\odot} \text{ yr}^{-1}$  to  $100 M_{\odot} \text{ yr}^{-1}$  within  $\sim 10 \text{ Myr}$ . Thus, the current SFR sets a relatively strong constraint for the time at which we observe the galaxy.

From exploring the orbital parameter space of this merger, we recognise there are numerous ways to match the features of Haro 11 and, thus, many possible formation scenarios. However, to find a set of parameters that produce several key aspects of the galaxy is not trivial. This is the first time Haro 11 has ever been simulated with hydrodynamical simulations, and that our simulations match several observed Haro 11 features is thus highly encouraging. Furthermore, it validates the hypothesis that Haro 11 is produced through a merger, and offers a specific possible merger setup. Future work, applying

more precise constraints and comparing other aspects of the galaxy, would be helpful to reduce the available parameter space.

## 6.2 Future work and improvements

The fiducial model and simulation suite presented in this paper show a great match between various properties of Haro 11 and, more widely, offers a basis for modelling the Haro 11 galaxy, and other BCGs. By building and improving on this model, the comparison with observations can be done in more detail, help understand the origin of other features, and possibly allow more quantitative analysis. However, even minimal improvements require substantial work and therefore left for future investigations. Here we highlight a few improvements that could be made.

There are certain properties of the progenitor galaxies that could be tweaked without significantly changing the orbit. For example, the initial bulge masses we use here are almost an order of magnitude higher than what is suggested through dynamical reasoning (Ö15) for the knots. We performed simple tests to check the impact of lowering the mass of the bulge, as well as removing it entirely. We find that the overall SFR remains largely unchanged, but that heavier bulges form more stars towards the centre (see also Mihos & Hernquist 1996), thus it could change the relative mass between stellar populations within the knots. Additionally, there is room to alter the gas masses, as they primarily impact the SFR and density of the tidal tails.

The relative position between the knots could be improved by changing the inclination of the prograde disc (associated with knot B and A), such that the disc arm (which we have shown can represent knot A) falls better in place where knot A is expected. This is a relatively minor change in the parameters, and we have noted that the tidal tail is stable to the small variations required to shift the disc arm by  $\sim 1 \text{ kpc}$ . However, this is not guaranteed as the inclination of the prograde galaxy is strongly connected to the morphology of the tidal tail and could worsen this match; or even another property, through complex dynamics.

Additionally, we were not able to conclusively exclude that one of the progenitor galaxies (i.e. the retrograde) is an elliptical galaxy. Our tests of this scenario showed that the overall SFR over time would drop, along with the stellar populations within knot C. However, this can be adjusted, if needed, by changing other parameters, such as the prograde gas fraction or orbital parameters.

Finally, we will explore this same Haro 11 model at a higher spatial resolution in Ejdetjärn et al. (in prep.), where we will focus on the escape of LyC and Ly $\alpha$  radiation and stellar cluster formation during a galaxy merger. We will employ post processing radiative transfer and evaluate the covering fraction to understand the impact of gas stripping and stellar feedback.

## 7 CONCLUSIONS

In this paper we have explored possible formation scenarios for the Haro 11 galaxy through numerical simulations of mergers between two galaxies. We perform a large suite of  $\sim 500$  hydrodynamical simulations by varying parameters that regulate the orbit and galactic properties of two disc galaxies. By using observational data as constraints, we are able to develop a fiducial Haro 11 model that show a broad agreement with several different observed features. Additionally, we present observations of the first direct detection of a stellar tidal tail in Haro 11.

Our main findings are as follows:

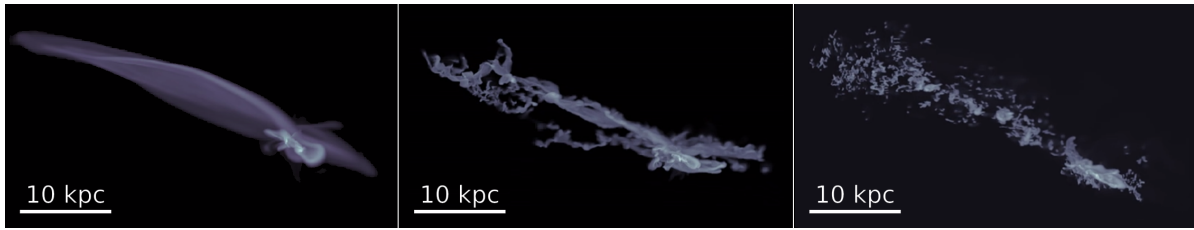


**Figure 14.** Density maps of the tidal tail in low-resolution simulations of varying circumgalactic density. From left to right, the densities are:  $\log_{10} \rho_{\text{CGM}} = (-6, -5, -4) \text{ m}_\text{H} \text{ cm}^{-3}$ .

(i) The orbital and galactic parameters of the progenitor galaxies interact in a complex manner that affects the final morphology, SFR, and stellar properties. We have highlighted how specific parameter changes can alter the merger scenario, and thus the final properties, of Haro 11. However, we find that the orbits are stable to small parameter variations and, thus, minor improvements could be made through tweaking the fiducial model further.

(ii) To produce the distinct *single* tidal tail observed in Haro 11, one of the progenitor galaxies needs to have a retrograde motion with the orbit. This weakens the second tidal tail, but to render it completely undetectable the galaxies need to be asymmetric; the retrograde needs to be either smaller, have less gas, or be more massive/dense (to overcome the gravitational pull from tidal forces). Other setups could also produce the one tidal tail, but many would likely show a mismatch for other features.

(iii) For our fiducial setup, we are able to reproduce the following qualities of Haro 11:

- The length, kinematics, and relative mass fraction of the HI tidal tail.
- The inner stellar and gaseous morphology. In particular, we show that the three stellar knots in Haro 11 can be found within our simulation.
- The  $\text{H}\alpha$  velocity field of the galaxy shows several similar qualities to the observed  $\text{H}\alpha$  kinematics. However, the speeds are notably larger than observed.
- The stellar cluster mass and age distributions. However, the ages are more uncertain, as the simulations suggest the observed population  $\lesssim 100$  Myr should be slightly older (to overlap with the starburst from the first interaction).

(iv) Accepting our fiducial model as a possible formation scenario for Haro 11, we are able to hypothesise about the origin of specific observed components:

- The two progenitor galaxies that form Haro 11 are currently undergoing their second close interaction and will fully merge within a few tens of Myr.
- In order for the tidal tail to expand to the observed length of 40 kpc, our simulations require 200 – 250 Myr between the first and second interaction.
- The inner morphology of the galaxy is made up from a gaseous disc, which is interacting in a prograde motion and having its disc stripped to form a tidal tail.
- The prograde galaxy has its centre where we would expect knot B, and its progenitor is a disc galaxy.
- An arm from the stellar and gas disc reaches down to form the diffuse stellar clusters that make up knot A. This arm also makes up the ‘ear’ that goes from knot A to the right of knot B.
- Knot C contains mainly old stars ( $\sim 100$  Myr) and its progenitor is likely a gas-poor galaxy.

- The galaxy centres will merge and become indistinguishable within 10 – 20 Myr, creating another brief starburst period.

In summary, our simulations demonstrate that a two-disc galaxy merger can replicate the observed features of Haro 11 (as hypothesised in Ö15), including its tidal tail, starburst activity, and stellar morphology. This supports the hypothesis that mergers play a central role in the formation of compact, starburst galaxies like Haro 11. While degeneracies remain in the parameter space, our results provide a strong foundation for future studies exploring the detailed mechanisms driving star formation and LyC escape in merging systems. Advancing this work with higher-resolution models and more precise observational constraints will further refine our understanding of galaxy evolution in extreme environments.

## ACKNOWLEDGEMENTS

The computations and data handling were enabled by resources provided by the National Academic Infrastructure for Supercomputing in Sweden (NAISS), partially funded by the Swedish Research Council through grant agreement no. 2022-06725. We made use of the medium computation allocations and small storage allocation.

OA acknowledges support from the Knut and Alice Wallenberg Foundation, the Swedish Research Council (grant 2019-04659), and the Swedish National Space Agency (SNSA Dnr 2023-00164).

FR acknowledges support provided by the University of Strasbourg Institute for Advanced Study (USIAS), within the French national programme Investment for the Future (Excellence Initiative) IdEx-Unistra.

The MEERKAT telescope is operated by the South African Radio Astronomy Observatory, which is a facility of the National Research Foundation, an agency of the Department of Science and Innovation.

For our analysis we have used PYTHON, including packages: numpy (Harris et al. 2020), matplotlib for PYTHON (Hunter 2007). Loading and analysis of the simulation data was done using tools from the yt-project (Turk et al. 2011).

## DATA AVAILABILITY

The data underlying this article will be shared on reasonable request to the corresponding author.

## REFERENCES

- Adamo A., Östlin G., Zackrisson E., Hayes M., Cumming R. J., Micheva G., 2010, *MNRAS*, **407**, 870  
 Adamo A., Östlin G., Zackrisson E., Hayes M., 2011, *MNRAS*, **414**, 1793  
 Agertz O., Kravtsov A. V., 2015, *ApJ*, **804**, 18

Agertz O., Kravtsov A. V., 2016, *ApJ*, **824**, 79  
 Agertz O., Kravtsov A. V., Leitner S. N., Gnedin N. Y., 2013, *ApJ*, **770**, 25  
 Agertz O., et al., 2021, *MNRAS*, **503**, 5826  
 Asplund M., Grevesse N., Sauval A. J., Scott P., 2009, *ARA&A*, **47**, 481  
 Behroozi P., Wechsler R. H., Hearin A. P., Conroy C., 2019, *MNRAS*, **488**, 3143  
 Bekki K., 2008, *MNRAS*, **388**, L10  
 Bergvall N., Östlin G., 2002, *A&A*, **390**, 891  
 Bergvall N., Zackrisson E., Andersson B. G., Arnberg D., Masegosa J., Östlin G., 2006, *A&A*, **448**, 513  
 Bergvall N., Leitner E., Zackrisson E., Marquart T., 2013, *A&A*, **554**, A38  
 Chabrier G., 2003, *Publications of the Astronomical Society of the Pacific*, **115**, 763  
 Chandar R., et al., 2023, *ApJ*, **949**, 116  
 Condon J. J., Darling J., Kovalev Y. Y., Petrov L., 2017, *ApJ*, **834**, 184  
 Cormier D., et al., 2014, *A&A*, **564**, A121  
 Danehkar A., Silich S., Herenz E. C., Östlin G., 2024, *A&A*, **689**, A333  
 Duc P.-A., Renaud F., 2013, in Souchay J., Mathis S., Tokieda T., eds., Vol. 861, *Lecture Notes in Physics*, Berlin Springer Verlag., p. 327, doi:10.1007/978-3-642-32961-6\_9  
 Eisenstein D. J., Hut P., 1998, *ApJ*, **498**, 137  
 Ejdetjärn T., Agertz O., Östlin G., Renaud F., Romeo A. B., 2022, *MNRAS*, **514**, 480  
 Ejdetjärn T., Agertz O., Östlin G., Rey M. P., Renaud F., 2024, *MNRAS*, **534**, 135  
 Gao Y., et al., 2022, *A&A*, **661**, A136  
 Grisdale K., Agertz O., Renaud F., Romeo A. B., Devriendt J., Slyz A., 2019, arXiv e-prints,  
 Gross A. C., Prestwich A., Kaaret P., 2021, *MNRAS*, **505**, 610  
 Harris C. R., et al., 2020, *Nature*, **585**, 357–362  
 Hayes M., Östlin G., Atek H., Kunth D., Mas-Hesse J. M., Leitherer C., Jiménez-Bailón E., Adamo A., 2007, *MNRAS*, **382**, 1465  
 Hernquist L., 1990, *ApJ*, **356**, 359  
 Hunter J. D., 2007, *Computing in Science & Engineering*, **9**, 90  
 Karl S. J., Naab T., Johansson P. H., Kotarba H., Boily C. M., Renaud F., Theis C., 2010, *ApJ*, **715**, L88  
 Kennicutt Jr. R. C., 1998, *ARA&A*, **36**, 189  
 Kim C.-G., Ostriker E. C., 2015, *ApJ*, **802**, 99  
 Komarova L., et al., 2024, *ApJ*, **967**, 117  
 Kostyuk I., Ciardi B., 2024, arXiv e-prints, p. arXiv:2412.04348  
 Lahén N., Johansson P. H., Rantala A., Naab T., Frigo M., 2018, *MNRAS*, **475**, 3934  
 Le Reste A., et al., 2024, *MNRAS*, **528**, 757  
 Leicester B., Bekki K., Tsujimoto T., 2024, arXiv e-prints, p. arXiv:2410.19257  
 MacHattie J. A., Irwin J. A., Madden S. C., Cormier D., Rémy-Ruyer A., 2014, *MNRAS*, **438**, L66  
 Machado R. E. G., Tissera P. B., Lima Neto G. B., Sodr e L., 2018, *A&A*, **609**, A66  
 Madden S. C., et al., 2013, *PASP*, **125**, 600  
 Menacho V., et al., 2019, *MNRAS*, **487**, 3183  
 Menacho V., et al., 2021, *MNRAS*, **506**, 1777  
 Michel-Dansac L., Blaizot J., Garel T., Verhamme A., Kimm T., Trebitsch M., 2020, *A&A*, **635**, A154  
 Micheva G., et al., 2013, *A&A*, **556**, A10  
 Mihos J. C., Hernquist L., 1996, *ApJ*, **464**, 641  
 Miki Y., Umemura M., 2018, *MNRAS*, **475**, 2269  
 Navarro J. F., Frenk C. S., White S. D. M., 1996, *ApJ*, **462**, 563  
 Östlin G., Amram P., Masegosa J., Bergvall N., Boulesteix J., 1999, *A&AS*, **137**, 419  
 Östlin G., Amram P., Bergvall N., Masegosa J., Boulesteix J., Márquez I., 2001, *A&A*, **374**, 800  
 Östlin G., Hayes M., Kunth D., Mas-Hesse J. M., Leitherer C., Petrosian A., Atek H., 2009, *AJ*, **138**, 923  
 Östlin G., Marquart T., Cumming R. J., Fathi K., Bergvall N., Adamo A., Amram P., Hayes M., 2015, *A&A*, **583**, A55  
 Östlin G., et al., 2021, *ApJ*, **912**, 155  
 Papaderos P., Östlin G., 2023, arXiv e-prints, p. arXiv:2312.13358

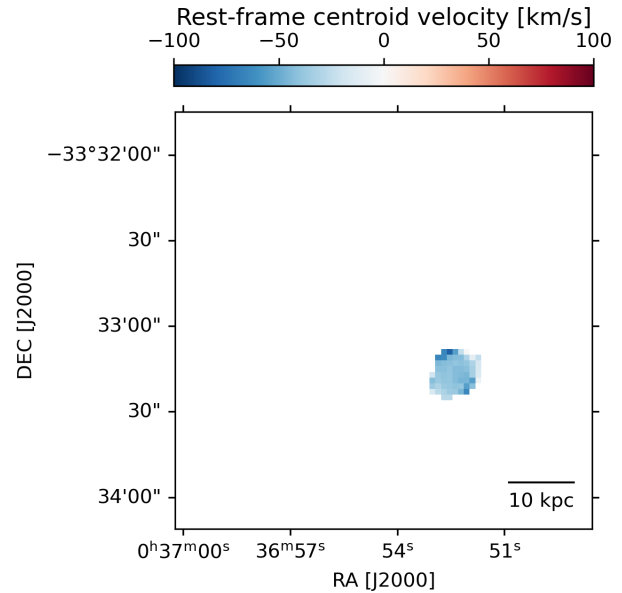


**Figure A1.** MEERKAT observations of the 21-cm line in absorption (Le Reste et al. 2024).

Pardy S. A., Cannon J. M., Östlin G., Hayes M., Bergvall N., 2016, *AJ*, **152**, 178  
 Pearson S., et al., 2018, *MNRAS*, **480**, 3069  
 Planck Collaboration et al., 2020, *A&A*, **641**, A6  
 Prestwich A. H., Jackson F., Kaaret P., Brorby M., Roberts T. P., Saar S. H., Yukita M., 2015, *ApJ*, **812**, 166  
 Privon G. C., Barnes J. E., Evans A. S., Hibbard J. E., Yun M. S., Mazzarella J. M., Armus L., Surace J., 2013, *ApJ*, **771**, 120  
 Renaud F., Bournaud F., Kraljic K., Duc P. A., 2014a, *MNRAS*, **442**, L33  
 Renaud F., Bournaud F., Kraljic K., Duc P. A., 2014b, *MNRAS*, **442**, L33  
 Renaud F., Bournaud F., Duc P.-A., 2015, *MNRAS*, **446**, 2038  
 Renaud F., Bournaud F., Agertz O., Kraljic K., Schinnerer E., Bolatto A., Daddi E., Hughes A., 2019, *A&A*, **625**, A65  
 Rivera-Thorsen T. E., Östlin G., Hayes M., Puschnig J., 2017, *ApJ*, **837**, 29  
 Schmidt M., 1959, *ApJ*, **129**, 243  
 Sirressi M., et al., 2022, *MNRAS*, **510**, 4819  
 Teyssier R., 2002, *A&A*, **385**, 337  
 Toro E. F., Spruce M., Speares W., 1994, *Shock Waves*, **4**, 25  
 Turk M. J., Smith B. D., Oishi J. S., Skory S., Skillman S. W., Abel T., Norman M. L., 2011, *ApJS*, **192**, 9  
 Zhang H.-X., et al., 2020, *ApJ*, **900**, 152

## APPENDIX A: HI VELOCITY MAP OF THE ABSORPTION

The velocity map of neutral HI emission presented in Figure 3 shows emission in both the inner parts and tidal tail. Meanwhile, the absorption presented here in Figure A1 shows significant absorption only in the inner parts of the galaxy. Furthermore, it indicates that there is a large outflow of neutral gas at velocities  $\sim 50 \text{ km s}^{-1}$  towards us.

This paper has been typeset from a  $\text{\LaTeX}$  file prepared by the author.